INTERNATIONAL JOURNAL FOR NUMERICAL METHODS IN FLUIDS
Int. J. Numer. Meth. Fluids (2011)
Published online in Wiley Online Library (wileyonlinelibrary.com). DOI: 10.1002/fld.2690

Numerical study of breaking waves by a two-phase flow model

Zhihua Xie*,†

Centre for Computational Fluid Dynamics, University of Leeds, Leeds, LS2 9JT, UK

SUMMARY

A two-phase flow model, which solves the flow in the air and water simultaneously, is presented for modelling breaking waves in deep and shallow water, including wave pre-breaking, overturning and post-breaking processes. The model is based on the Reynolds-averaged Navier–Stokes equations with the $k-\epsilon$ turbulence model. The governing equations are solved by the finite volume method in a Cartesian staggered grid and the partial cell treatment is implemented to deal with complex geometries. The SIMPLE algorithm is utilised for the pressure-velocity coupling and the air-water interface is modelled by the interface capturing method via a high resolution volume of fluid scheme. The numerical model is validated by simulating overturning waves on a sloping beach and over a reef, and deep-water breaking waves in a periodic domain, in which good agreement between numerical results and available experimental measurements for the water surface profiles during wave overturning is obtained. The overturning jet, air entrainment and splash-up during wave breaking have been captured by the two-phase flow model, which demonstrates the capability of the model to simulate free surface flow and wave breaking problems. Copyright © 2011 John Wiley & Sons, Ltd.

Received 2 May 2011; Revised 17 August 2011; Accepted 23 August 2011

KEY WORDS: breaking waves; two-phase flow model; Reynolds-averaged Navier–Stokes (RANS) equations; VOF method; Cartesian cut cell method; turbulence modelling

1. INTRODUCTION

Wave breaking plays an important role in air-sea interaction, surf zone dynamics, nearshore sediment transport, marine hydrodynamics and wave-structure interaction. The process of wave breaking on a beach is one of the most common phenomena seen in nature. Wave breaking is responsible for the wave energy dissipation and the generation of turbulence, vorticity and nearshore currents in the surf zone. Over the last three decades, significant advances have been made in the theoretical, experimental and numerical studies of the characteristics of breaking waves. Some excellent reviews of breaking waves and wave mechanics can be found in [1–4].

Much of our knowledge of breaking waves comes from laboratory measurements. Several systematic studies have been done for steady breaking waves [5], quasi-steady breaking waves [6], unsteady deep-water breaking waves [7–11] and breaking waves in the laboratory surf zone [12–14]. Overall, with the development of measurement techniques, physical experiments have provided much insight into the kinematics and dynamics of breaking waves. However, the process of wave breaking has not yet been fully understood because of its complexity and experimental investigations still struggle to provide the detailed flow field, especially during wave overturning in three dimensions. Moreover, conducting physical experiments cost a lot of money and are also very time-consuming. Thus, a variety of numerical studies, which are cost-effective and can provide the detailed flow field, act as a complementary approach to study breaking waves.

*Correspondence to: Zhihua Xie, Hydro-environmental Research Centre, School of Engineering, Cardiff University, Cardiff, CF24 3AA, UK.
†E-mail: zhihua.xie@hotmail.com

There are a variety of numerical simulations for breaking waves, such as the shallow water model [15, 16], Boussinesq model [17] and fully nonlinear potential flow model [18–21]. Although the depth-integrated models (shallow water and Boussinesq models) are widely used in modelling surface wave propagation, they cannot capture the realistic wave breaking and overturning processes. The fully nonlinear potential flow model, which is based on inviscid and irrotational assumptions, is capable of simulating breaking waves and can provide insight into the kinematics and dynamics of water waves during wave overturning. However, this model usually terminates before the plunging jet touches down and cannot provide any information after wave breaking. With the development of the numerical methods for the Navier–Stokes equations and free surface flows [22], several numerical studies have been performed to further our understanding of breaking waves, such as the steady spilling breaker generated by submerged bodies [23–25], deep-water breaking waves [26–29] and breaking waves in the surf zone [30–36]. In order to track or capture the interface, several techniques have been developed, such as the marker-and-cell method [23, 33], surface tracking method [24], volume of fluid (VOF) method [26, 28, 30–32, 37], level set method [27, 29] and the density function method [34]. In addition, there are some meshless methods such as the moving particle semi-implicit method [38] , smoothed particle hydrodynamics method [39–41], and Meshless Local Petrov-Galerkin method based on Rankine source solution (MLPG_R) method [42]. It is worth mentioning that most models are based on one-phase flow, in which only the flow in water is considered in the computation, the pressure in the air is taken as a constant, and the boundary conditions are specified at the free surface. During wave breaking, these one-phase flow models may be inadequate to deal with the air entrainment and splash-up process. Additional complication arises in the treatment of boundary conditions at the highly distorted free surface. Thus, in order to take the air into account for wave breaking, recently, several two-phase flow models, in which both flows in the air and water are solved, have been developed to study the details of breaking waves and the air entrainment during wave breaking in deep water [26–29], breaking solitary waves on sloping beaches [37] and breaking waves in the surf zone [35, 36]. From the discussion earlier, it is shown that two-phase flow model is preferable to study the kinematics and dynamics of water waves during wave breaking.

The objective of this paper is to study breaking waves in deep and shallow water, focusing on the wave overturning and post-breaking processes. In this study, a two-phase flow model, which solves the flow in the air and water simultaneously, has been developed for modelling breaking waves and providing detailed phenomena during wave overturning. The model is based on the Reynolds-averaged Navier–Stokes (RANS) equations with the $k-\epsilon$ turbulence model. The governing equations are solved by the finite volume method in a Cartesian staggered grid and the partial cell treatment is implemented to deal with complex geometries. The SIMPLE algorithm [43] is utilised for the pressure-velocity coupling and the air-water interface is modelled by the interface capturing method via a high resolution VOF scheme developed by Ubbink [44].

The organisation of this paper is as follows. The description of the mathematical model for the two-phase flow is described in § 2. The numerical method and implementation are presented in § 3. The numerical model is validated by simulating overturning waves on a sloping beach and over a reef, and deep-water breaking waves in a periodic domain in § 4. Finally, conclusions are drawn in § 5.

2. MATHEMATICAL MODEL

2.1. Governing equations

The governing equations for incompressible Newtonian fluid flow are the RANS equations. Mass conservation is described by the continuity equation

$$\frac{\partial \rho}{\partial t} + \nabla \cdot (\rho \boldsymbol{u}) = 0, \tag{1}$$

where ρ is the density, t is the time and $\boldsymbol{u} = (u, w)$ is the velocity vector.

DOI: 10.1002/fld

If we assume that the fluid is incompressible ($\mathrm{d}\rho/\mathrm{d}t = 0$), then the continuity equation can be simplified to

$$\nabla \cdot \boldsymbol{u} = 0. \tag{2}$$

The momentum conservation is expressed as

$$\frac{\partial(\rho \boldsymbol{u})}{\partial t} + \nabla \cdot (\rho \boldsymbol{u} \otimes \boldsymbol{u}) = -\nabla p + \nabla \cdot [(\mu + \mu_t)(\nabla \boldsymbol{u} + \nabla^{\mathrm{T}} \boldsymbol{u})] + \rho \boldsymbol{g}, \tag{3}$$

where p represents pressure, $\boldsymbol{g}$ the gravitational acceleration vector, μ the dynamic viscosity of the fluid, and $\mu_t = \rho C_\mu k^2/\epsilon$ is the turbulent eddy viscosity. k is turbulent kinetic energy and ϵ is turbulent eddy dissipation which are governed by the $k-\epsilon$ turbulence model [45]

$$\frac{\partial(\rho k)}{\partial t} + \nabla \cdot (\rho \boldsymbol{u} k) = \nabla \cdot [(\mu + \frac{\mu_t}{\sigma_k})\nabla k] + P_k - \rho\epsilon, \tag{4}$$

$$\frac{\partial(\rho \epsilon)}{\partial t} + \nabla \cdot (\rho \boldsymbol{u} \epsilon) = \nabla \cdot [(\mu + \frac{\mu_t}{\sigma_\epsilon})\nabla \epsilon] + C_{1\epsilon}\frac{\epsilon}{k}P_k - C_{2\epsilon}\rho\frac{\epsilon^2}{k}, \tag{5}$$

where $P_k = \mu_t(\partial u_i/\partial x_j + \partial u_j/\partial x_i)^2/2$ is the turbulent production term, and the empirical coefficients C_μ, σ_k, σ_ϵ, $C_{1\epsilon}$ and $C_{2\epsilon}$ are given in Table I.

The momentum equation is closed with the constitutive relations for the density and dynamic viscosity of the fluid

$$\rho = F\rho^{\mathrm{w}} + (1-F)\rho^{\mathrm{a}}, \tag{6}$$

$$\mu = F\mu^{\mathrm{w}} + (1-F)\mu^{\mathrm{a}}, \tag{7}$$

where the superscripts w and a denote fluid water and air, respectively. F is the volume fraction defined as

$$F = \begin{cases} 1, & \text{if only water is present;} \\ 0, & \text{if only air is present.} \end{cases} \tag{8}$$

The air-water interface is then within the cells where $0 < F < 1$. A particle on surface stays on surface and the volume fraction F has a zero material derivative

$$\frac{\mathrm{d}F}{\mathrm{d}t} = \frac{\partial F}{\partial t} + \boldsymbol{u} \cdot \nabla F = 0. \tag{9}$$

These equations complete the mathematical description of the two-phase flow model.

2.2. *Initial and boundary conditions*

In order to completely describe the mathematical model, it is necessary to define the boundary conditions in a computational domain. The no-slip boundary condition is imposed on the solid boundary, and the law of the wall function is applied for the $k-\epsilon$ turbulence model. For the outlet, the zero-gradient boundary conditions are applied for the flow. As both fluids in the air and water are solved simultaneously in the present two-phase flow model, the kinematic and dynamic free surface boundary conditions are already implemented, and they do not need to be specified explicitly at the air-water interface. The inlet boundary conditions are case-dependent. In general, the time history

Table I. Empirical coefficients in the $k-\epsilon$ turbulence model [45].

C_μ	σ_k	σ_ϵ	$C_{1\epsilon}$	$C_{2\epsilon}$
0.09	1.0	1.3	1.44	1.92

DOI: 10.1002/fld

of the velocity field and the volume fraction at the inlet are obtained from an analytical solution of water waves. For the turbulence field, the method of Lin [46] is adopted here. The turbulent kinetic energy is obtained as $k = \frac{1}{2}(I \times C)^2$, where C is the wave phase speed and I is the turbulent intensity. The turbulent eddy dissipation $\epsilon = \rho C_\mu k^2/(I_\epsilon \times \mu)$ is adjusted, so the turbulent eddy viscosity is I_ϵ times the dynamic viscosity of each fluid at the inlet. Unless stated otherwise $I = 0.005$ and $I_\epsilon = 10$ are used in this study.

In the computation, the initial flow field at $t = 0$ has to be prescribed. For calculations with the fluids initially at rest, the flow field is initialised with zero velocity and hydrostatic pressure, and the volume fraction is computed from the initial water depth. When the wave is initialised in the computational domain, the water velocities and water surface are specified using the corresponding analytical solution for water waves. The velocity in the air is initialised as zero in this case as little is known about the flow in the air, and the pressure distribution in the whole domain is hydrostatic.

3. NUMERICAL METHOD

In order to solve the mathematical model proposed in the previous section, a numerical discretisation method is needed. There are several discretisation approaches for numerical solution of partial differential equations, such as the finite difference method, finite element method, meshless methods, and the finite volume method (FVM). In this study, the FVM is used to discretise the governing equations on a staggered Cartesian grid, which has the advantage of strong coupling between the velocity and the pressure. Figure 1 shows a typical variable arrangement in a 2D Cartesian grid, in which the velocities are located on the face centre of the control volume, and the pressure, all other scalar variables and the volume fraction F are stored at the cell centre. P is the present node, the upper-case letter E, W, N and S denote neighbouring nodes on the east, west, north and south with respect to the central node P. The lower-case e, w, n and s denote the corresponding face of the control volume, whereas c denotes the centre of the control volume.

3.1. Finite volume discretisation

In the FVM, also known as the control volume method, the whole domain is divided into a number of control volumes, such that there is a control volume surrounding each grid point. The differential equation is integrated over each control volume in order to derive the algebraic equation containing the grid-point values of ϕ, where ϕ is the considered variable. The discretised equation expresses

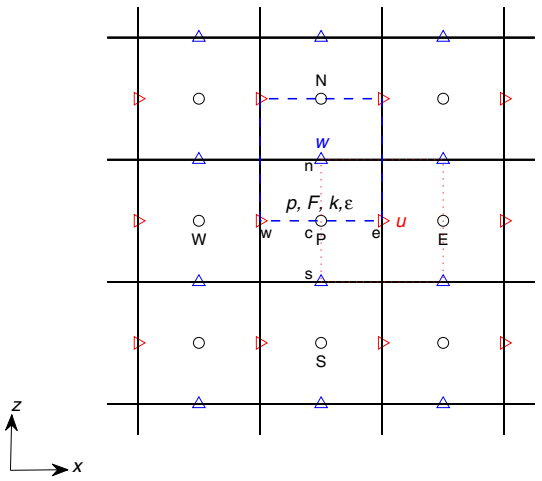

Figure 1. Variables used for the control volume (i,k) in a 2D staggered Cartesian grid. Velocities u(i,k) (▷) and w(i,k) (△) are stored at the centre of the east and north face of the continuity control volume. Pressure and other variables ϕ(i,k) (○) are stored at the centre of the continuity control volume. The control volume for velocities u (dotted line) and w (dashed line) are also shown.

DOI: 10.1002/fld

the conservation principle for a finite control volume, just as the differential equation expresses it for an infinitesimal control volume. The FVM is conservative and can deal with complex geometries [47, 48], thus it is especially suitable for modelling free surface flows because of the requirement of mass conservation and the deformed interface, therefore it is adopted in the present study.

Consider a volume of fluid Ω that has an arbitrary domain, the surface of the control volume is S and the unit outward normal vector to the face f is $\boldsymbol{n}$. All the governing equations can be recast into a general integral formulation as below

$$\int_\Omega \frac{\partial}{\partial t}(\rho\phi)\mathrm{d}\Omega + \int_S (\rho \boldsymbol{u}\cdot\boldsymbol{n})\phi \mathrm{d}S = \int_S \Gamma \frac{\partial \phi}{\partial n}\mathrm{d}S + \int_\Omega Q_\phi^{\mathrm{S}}\mathrm{d}\Omega, \tag{10}$$

where ϕ denotes the dependent variable, Γ is the viscosity and Q_ϕ^{S} is the source term in the control volume.

Table II shows the various values of ϕ, Γ and Q_ϕ^{S} in the general integral formulation to represent the the Reynolds-averaged Navier–Stokes equations. It is noted that the final form of the continuity Equation (2) used here is obtained under the assumption that the fluid is incompressible.

3.2. The complex geometry treatment in Cartesian grids

To deal with complex geometries in engineering applications, overlapping grids, boundary-fitted grids and unstructured grids can be used. Unstructured grids provide great flexibility to conform onto complex stationary or moving boundaries and can easily refine or coarsen meshes in a region of the domain depending on the flow feature. However, they require additional computational efforts and further complicate the algorithm implementation as there is no pre-define order of the control volumes and their geometric layouts need to be calculated. Furthermore, generating high quality boundary-fitted or unstructured grids is usually very cumbersome. Cartesian grid methods, which can simulate flow with complex geometries on Cartesian grids, avoid these problems. The most popular methods are the immersed boundary method [49–52] and Cartesian cut cell method [53–58]. The primary advantage of the Cartesian grid method is that only little modification of the programme on Cartesian grids is needed to account for the complex geometries. It also has the advantage of simplified grid generation and simulating flow with moving boundaries because of the use of stationary, nondeforming grids. The drawback of these methods is that implementing boundary conditions is not straightforward and instability problems may occur in small cells when explicit schemes are used. Thus, the cell-merging technique [59] and using slightly different control volumes [60] are developed to avoid this instability, both of which effectively increase the size of the cut cell.

In this study, the partial cell treatment is used and a typical θ function in a control volume, arises from Fractional-Area-Volume Obstacle Representation method [61], is introduced in the finite volume discretisation. A similar approach can be found in [62] for simulating a moving body in free surface flows. The θ function is defined whose value is 1 for a point accessible to fluid and 0 for a point inside an obstacle. The average of this function over a control volume or cell face is the fraction of the volume or area available to the flow. Figure 2 shows a typical cut cell in a 2D Cartesian grid. It is worth mentioning that, in Lin's work [62], the partial cell treatment is based on the finite difference discretisation and an explicit scheme. However, in the present method, to

Table II. Values of ϕ, Γ and Q_ϕ^{S} in the general integral formulation to represent the Reynolds-averaged Navier–Stokes equations.

Equation	ϕ	Γ	Q_ϕ^{S}
Continuity	1	0	0
Momentum	$\boldsymbol{u}$	$\mu+\mu_t$	$-\nabla p+\rho\boldsymbol{g}$
k	k	$\mu+\frac{\mu_t}{\sigma_k}$	$P_k-\rho\epsilon$
ϵ	ϵ	$\mu+\frac{\mu_t}{\sigma_\epsilon}$	$C_{1\epsilon}\frac{\epsilon}{k}P_k-C_{2\epsilon}\rho\frac{\epsilon^2}{k}$

DOI: 10.1002/fld

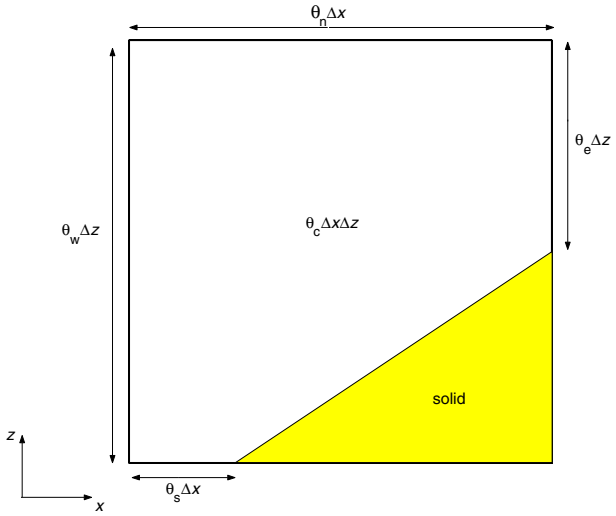

Figure 2. θ function for a typical cut cell in a 2D Cartesian grid, in which the length of the face is represented as $\theta \cdot \Delta x$ or $\theta \cdot \Delta z$, and the volume of the cell is represented by $\theta_c \cdot \Delta x \Delta z$.

prevent the instability in small cells, an implicit scheme for time integration is employed for the governing equations together with the finite volume discretisation.

In contrast to a full cell, the convective and diffusive fluxes at cell faces are modified in a cut cell, which will be presented in the following discretisation.

3.3. Spatial discretisation

3.3.1. Convection term. The finite volume discretisation of the convection term is obtained as

$$\begin{aligned} Q_\phi^{\mathrm{C}} = \int_S (\rho \boldsymbol{u} \cdot \boldsymbol{n}) \phi \mathrm{d}S &= \sum_{\mathrm{f}} (\theta A)_{\mathrm{f}} \left[(\rho \boldsymbol{u} \cdot \boldsymbol{n}) \phi \right]_{\mathrm{f}} \\ &= \sum_{\mathrm{f}} (\rho \boldsymbol{u} \cdot \boldsymbol{n} \theta A)_{\mathrm{f}} \phi_{\mathrm{f}} \\ &= \sum_{\mathrm{f}} m_{\mathrm{f}} \phi_{\mathrm{f}}, \end{aligned} \tag{11}$$

where the subscript f denotes the corresponding face of the control volume, A is the area of the face and m is the mass flux through the face

$$m = \rho \boldsymbol{u} \cdot \boldsymbol{n} \theta A. \tag{12}$$

In cut cells, the mass flux has also to be modified by the θ function on the boundary. If $\theta = 0$, there is no mass flux through the face and the convective flux is obtained as

$$m_{\mathrm{f}} = 0. \tag{13}$$

The mass flux at the faces of the momentum control volume can be obtained by the interpolation of values of ρ and $\boldsymbol{u}$, such as $m_{\mathrm{f}} = \rho_{\mathrm{f}} \boldsymbol{u}_{\mathrm{f}} \cdot \boldsymbol{n} \theta_{\mathrm{f}} A_{\mathrm{f}}$, however, the mass conservation in the momentum control volume can be only guaranteed to the accuracy of the interpolation procedure [47]. Thus, in this study, the m_{f} is obtained from the interpolation of the mass fluxes, which is already available at the faces of the continuity control volumes. The face value ϕ_{f} can be obtained from different schemes and will be described in detail as follows.

First order upwind scheme

The upwind scheme implies that the convection is received from upstream and transmitted to the next control volume downstream. In the first order upwind (FOU) scheme, the value of ϕ on the

DOI: 10.1002/fld

face of the control volume is taken by the constant extrapolation of the value of ϕ at the grid point of the donor cell, for example

$$\phi_{\mathrm{f}}^{\mathrm{FOU}} = \phi_{\mathrm{D}}, \tag{14}$$

where subscripts D, A, and U denote donor cell, acceptor cell and upwind cell, which is shown in Figure 3.

If the first order upwind scheme is used, the convection term in the east face of the control volume can be expressed as

$$m_{\mathrm{e}}\phi_{\mathrm{e}} = \max(m_{\mathrm{e}}, 0)\phi_{\mathrm{P}} - \max(-m_{\mathrm{e}}, 0)\phi_{\mathrm{E}}. \tag{15}$$

High order schemes

Among all the possible schemes, the first order upwind scheme has the best convergence property, but the aim of other schemes is to improve the accuracy. Thus, when a high order scheme is used, it is advantageous to also use the first order formulation, and the difference between the first order upwind and the other scheme gives rise to an additional source term Q_{ϕ}^{H}, used in the deferred correction approach [47].

In the second order upwind (SOU) scheme, the value at the face of the control volume is obtained by the linear extrapolation of the value of ϕ at two upstream cells as

$$\begin{aligned} \phi_{\mathrm{f}}^{\mathrm{SOU}} &= \frac{3}{2}\phi_{\mathrm{D}} - \frac{1}{2}\phi_{\mathrm{U}} \\ &= \phi_{\mathrm{D}} + \frac{1}{2}(\phi_{\mathrm{D}} - \phi_{\mathrm{U}}) \\ &= \phi_{\mathrm{f}}^{\mathrm{FOU}} + \frac{1}{2}(\phi_{\mathrm{D}} - \phi_{\mathrm{U}}). \end{aligned} \tag{16}$$

High resolution scheme

It is well known that unphysical wiggles (numerical oscillations) will appear in numerical simulations with high order schemes under some circumstances. Thus, a high resolution scheme [48], which combines the high order accuracy with monotonicity, is used in this study to discretise the value at the face as

$$\phi_{\mathrm{f}}^{\mathrm{HRS}} = \phi_{\mathrm{f}}^{\mathrm{FOU}} + \Psi\left(r_{\mathrm{f}}^{\phi}\right)\left(\phi_{\mathrm{f}}^{\mathrm{SOU}} - \phi_{\mathrm{f}}^{\mathrm{FOU}}\right), \tag{17}$$

in which $\Psi()$ is the limiter function where the minmod limiter [63], which is one of the simplest second-order Total Variation Diminishing schemes, is used here

$$\Psi(r) = \max[0, \min(r, 1)]. \tag{18}$$

Similar results were obtained by using other limiter functions and a general review of various limiter functions can be found in [64] and will not be presented here. r_{f}^{ϕ} represents the ratio of successive gradients of ϕ on the solution mesh and obtained as

$$r_{\mathrm{f}}^{\phi} = \frac{\phi_{\mathrm{A}} - \phi_{\mathrm{D}}}{\phi_{\mathrm{D}} - \phi_{\mathrm{U}}}. \tag{19}$$

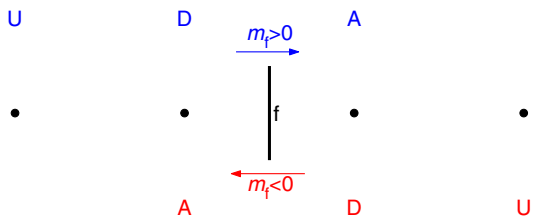

Figure 3. Notation of the cells for the interpolation at the face f: D, A and U denote donor cell, acceptor cell and upwind cell, respectively.

DOI: 10.1002/fld

Discussion

The convection term plays an important role in numerical solution of the Navier–Stokes equations. For a two-phase flow model, the convection term can be discretised in two different ways: conservative form and nonconservative form.

When nonconservative form is employed, the density in the centre of the control volume is used and the mass flux on the face m'_f can be obtained as

$$m'_f = \rho_c(\boldsymbol{u} \cdot \boldsymbol{n}\theta A)_f. \tag{20}$$

As we assume that the velocity does not vary discontinuously near an interface, the resulting mass flux is continuous in a control volume but discontinuous between the control volumes. Many people used the nonconservative form as it is simple for numerical implementation. However, the nonconservative form will violate the rule for consistency at control volume faces proposed by Patankar [43]:

> **Consistency at control volume faces:** when a face is common to two adjacent control volumes, the flux across it must be represented by the *same* expression in the discretisation equations for the two control volumes.

For example on the east face of the control volume P, the mass flux is expressed as $\rho_P(\boldsymbol{u} \cdot \boldsymbol{n}\theta A)_e$ when the control volume surrounding P is considered, and as $\rho_E(\boldsymbol{u} \cdot \boldsymbol{n}\theta A)_e$ when the control volume surrounding E is considered. In the vicinity of the interface, the mass flux across the face between the control volumes surrounding P and E will be inconsistent when $\rho_P \neq \rho_E$.

Therefore, the conservative form for the mass flux

$$m_f = (\rho \boldsymbol{u} \cdot \boldsymbol{n}\theta A)_f, \tag{21}$$

is employed in this study.

In the available literature, the conservative form is used in a few two-phase flow models [44, 65–68]. It is mentioned that special attention has to be paid in the discretisation of the conservative form of the convection term, otherwise, high and irregular velocities near the interface can sometimes destroy the solution [69], and one way to overcome this is to use the nonconservative form of the convection term [70]. In addition, special attention should be paid to the discretisation of the body force, otherwise non-physical velocities will be generated for the quiescent fluid [71,72].

The idea of consistency between mass and momentum conservation has been proposed in the conservative form [44, 67, 68]. For collocated grids, Ubbink [44] used the face value for F_f calculated from the VOF equation to obtain the mass flux for the momentum equation, whereas Bussmann [68] explicitly calculated the exact mass flux based on the volume tracking method. It is not easy to calculate consistent mass fluxes across cell faces for a staggered grid, Rudman [67] introduced a twice-as-fine sub-mesh nested within the underlying solver mesh for mass convection, in order to overlap the control volumes for the mass and momentum to get the consistency. Rudman [67] used the explicit scheme for the momentum equation and calculated the mass fluxes based on the volume fraction that was obtained from the Youngs' VOF method [73]. However, it is not clear yet how to deal with this consistency in a single staggered grid if the mass flux is not calculated based on the explicit interface advection (such as surface capturing methods) and especially when the implicit scheme is employed for the momentum equation.

It is worth remarking that the mass flux is discontinuous in a control volume in the conservative form because of the density variation between the cell face and cell centre (here the mass flux at the cell centre means the mass flux taken its corresponding values at the centre point). Sometimes, the combination of the conservative form and the high resolution scheme may lead to some convergence problems in the simulation. Thus, a step function for the mass flux is introduced to the high resolution scheme to get more robust and accurate solution as

$$\phi_f^{HRS} = \phi_f^{FOU} + \Phi\left(r_f^m\right)\Psi\left(r_f^\phi\right)\left(\phi_f^{SOU} - \phi_f^{FOU}\right), \tag{22}$$

where $\Phi()$ is the step function and r_f^m is the variation for the mass which is defined as the ratio of the mass flux between the conservative and nonconservative form

DOI: 10.1002/fld

$$r_{\mathrm{f}}^{m} = \frac{m_{\mathrm{f}}}{m_{\mathrm{f}}'}. \tag{23}$$

The step function $\Phi()$ takes the form

$$\Phi(r) = \begin{cases} 1, & \text{if } |r| \leqslant 1; \\ 0, & \text{otherwise,} \end{cases} \tag{24}$$

which means that the present high resolution scheme switches to the first order upwind scheme when the density on the cell face is larger than the density in the cell centre.

3.3.2. Diffusion term. The finite volume discretisation of the diffusion term is obtained as

$$Q_{\phi}^{\mathrm{D}} = \int_{S} \Gamma \frac{\partial \phi}{\partial n} \mathrm{d}S = \sum_{\mathrm{f}} \Gamma_{\mathrm{f}} \frac{\partial \phi}{\partial n} (\theta A)_{\mathrm{f}}, \tag{25}$$

where the viscosity on the face is obtained by the harmonic mean [43], for example, on the east face

$$\Gamma_{\mathrm{e}} = \frac{\Gamma_{\mathrm{P}} \Gamma_{\mathrm{E}}}{\lambda_{\mathrm{e}} \Gamma_{\mathrm{P}} + (1 - \lambda_{\mathrm{e}}) \Gamma_{\mathrm{E}}}, \tag{26}$$

where $\lambda_e = |eE|/|PE|$. Analogous expressions can be derived for all other faces (f = w, n, s) by making appropriate index substitutions and will not be shown here.

The gradient at the face is calculated by the finite difference approach as

$$\frac{\partial \phi}{\partial n} = \frac{\phi_{\mathrm{nb}} - \phi_{\mathrm{P}}}{\Delta_{\mathrm{Pnb}}}, \tag{27}$$

where Δ_{Pnb} is the distance from the present point P to the neighbouring point nb.

When the control volume is a cut cell, special attention has to be paid to the spatial discretisation. When the face of a momentum control volume is on the wall, the diffusion flux is obtained as

$$\int_{S} \Gamma \frac{\partial \phi}{\partial n} \mathrm{d}S = \sum_{\mathrm{f}} \Gamma_{\mathrm{f}} \frac{\partial \phi}{\partial n} (\theta A)_{\mathrm{f}} + \tau_{\mathrm{w}} [(1 - \theta) A]_{\mathrm{f}}, \tag{28}$$

where $\frac{\partial \phi}{\partial n}$ is calculated by the finite difference approach in Equation (27) and τ_{w} is the shear stress on the face of the control volume. For example, in the case of the control volume for u momentum equation in 2D (see Figure 4), the shear stress on the south face is

$$\tau_{\mathrm{w}} = -\Gamma_{\mathrm{s}} \frac{u_{\mathrm{P}} - u_{\mathrm{solid}}}{0.5(\theta^{u} \Delta z)}, \tag{29}$$

where u_{solid} is the velocity on the solid boundary.

3.3.3. Source term.

Source term linearisation
When the source term Q_{ϕ}^{S} is a function of ϕ, then there are many ways in which the Q_{ϕ}^{S0} and Q_{ϕ}^{S1} can be chosen to satisfy

$$Q_{\phi}^{\mathrm{S}} = Q_{\phi}^{\mathrm{S0}} + Q_{\phi}^{\mathrm{S1}} \phi, \quad Q_{\phi}^{\mathrm{S1}} < 0. \tag{30}$$

The term in Q_{ϕ}^{S} without ϕ goes into the term Q_{ϕ}^{S0}. The term that includes ϕ is modified as $Q_{\phi}^{\mathrm{S1}} \phi$ provided $Q_{\phi}^{\mathrm{S1}} < 0$ is satisfied, otherwise, it goes into the term Q_{ϕ}^{S0}. The advantage of this way is that once substituting the discretised source term into the governing equation, the term $Q_{\phi}^{\mathrm{S1}} \phi$ may be moved to left-hand side of the equation, yields an equation that has a stronger diagonal dominance, and therefore a better and faster rate of convergence will be achieved [43].

DOI: 10.1002/fld

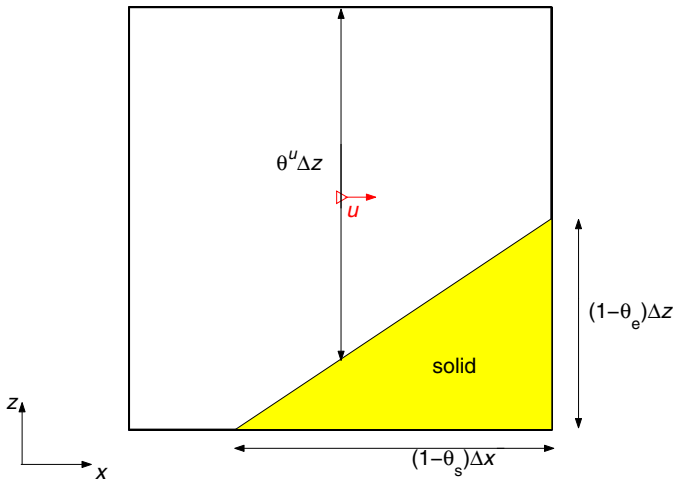

Figure 4. Boundary treatment in a cut cell for the u momentum equation in 2D Cartesian grid.

Pressure term

The finite volume discretisation of the pressure term is obtained as

$$Q_\phi^{\mathrm{p}} = \int_\Omega -\nabla p \mathrm{d}\Omega = -\nabla p \theta_{\mathrm{c}} \Omega, \tag{31}$$

and the pressure gradient is calculated as

$$\begin{aligned} \nabla p &= \left(\frac{\partial p}{\partial x}, \frac{\partial p}{\partial z} \right) \\ &= \left(\frac{p_{\mathrm{e}} - p_{\mathrm{w}}}{\Delta x}, \frac{p_{\mathrm{n}} - p_{\mathrm{s}}}{\Delta z} \right). \end{aligned} \tag{32}$$

Body force term

The finite volume discretisation of the body force term is obtained as

$$Q_\phi^{\mathrm{B}} = \int_\Omega \rho \boldsymbol{g} \mathrm{d}\Omega = \rho_{\mathrm{c}} \boldsymbol{g} \theta_{\mathrm{c}} \Omega, \tag{33}$$

where the value in the centre of the control volume is obtained by the volume averaging of two values on the face of the control volume.

3.4. Temporal discretisation

A backward finite difference is used for the time derivative, which leads to an implicit scheme for the governing equations

$$Q_\phi^{\mathrm{T}} = \int_\Omega \frac{\partial}{\partial t}(\rho\phi) \mathrm{d}\Omega = \frac{\rho_{\mathrm{c}}^{n+1}\phi^{n+1} - \rho_{\mathrm{c}}^{n}\phi^{n}}{\Delta t} \theta_{\mathrm{c}} \Omega, \tag{34}$$

where Δt is the time step and the superscripts $n+1$ and n mean the value in current and previous time step, respectively. The implicit scheme has the advantage of unconditional stability and thus can prevent the instability problem in small cut cells.

3.5. General form of the discretisation

Substituting all the above discretised terms into Equation (10) and subtracting the continuity Equation (1) multiplied by ϕ_{P}^{n+1}, leads to

$$a_{\mathrm{P}}^{\phi} \phi_{\mathrm{P}}^{n+1} = \sum a_{\mathrm{nb}}^{\phi} \phi_{\mathrm{nb}}^{n+1} + b_{\mathrm{P}}^{\phi}, \tag{35}$$

DOI: 10.1002/fld

where a^{ϕ} is the coefficient, the subscripts P and nb=E,W,N,S denote the variables in the present and neighbouring cells, respectively and b_{P}^{ϕ} is the source term.

In nonlinear problems, it is often desirable to slow down the change in the predicted change of the dependent variable and in such circumstances under-relaxation [43] is used, thus Equation (35) may be written as

$$\phi_{\mathrm{P}}^{n+1} = \phi_{\mathrm{P}}^{0} + \alpha_{\phi}\left(\frac{\sum a_{\mathrm{nb}}^{\phi}\phi_{\mathrm{nb}}^{n+1} + b_{\mathrm{P}}^{\phi}}{a_{\mathrm{P}}^{\phi}} - \phi_{\mathrm{P}}^{0}\right), \tag{36}$$

or

$$\frac{a_{\mathrm{P}}^{\phi}}{\alpha_{\phi}}\phi_{\mathrm{P}}^{n+1} = \sum a_{\mathrm{nb}}^{\phi}\phi_{\mathrm{nb}}^{n+1} + b_{\mathrm{P}}^{\phi} + \frac{1-\alpha_{\phi}}{\alpha_{\phi}}\phi_{\mathrm{P}}^{0}, \tag{37}$$

where ϕ_{P}^{0} is the value from the previous iteration and $0 < \alpha_{\phi} < 1$ is the under-relaxation factor. There are no general rules for choosing the best value for the under-relaxation factor [43], thus from our experience $\alpha_{\phi} = 0.7$ is used in this study.

The coefficients depend on the approximations used and the first order upwind scheme is used in this study as the basis of the formulation, high resolution scheme is implemented using the deferred correction method via source term Q_{ϕ}^{H} [47]. For example, the coefficients for momentum equation $\phi = u, w$ are

$$\begin{aligned} a_{\mathrm{nb}}^{\phi} &= \max(-m_{\mathrm{f}}^{\phi}, 0) + \frac{\Gamma_{\mathrm{f}}(\theta A)_{\mathrm{f}}}{\Delta_{\mathrm{Pnb}}}, \\ a_{\mathrm{P}}^{\phi} &= \frac{\rho_{\mathrm{c}}^{n}\theta_{\mathrm{c}}\Omega}{\Delta t} + \sum_{\mathrm{nb}} a_{\mathrm{nb}}^{\phi}, \\ b_{\mathrm{P}}^{\phi} &= Q_{\phi}^{\mathrm{p}} + Q_{\phi}^{\mathrm{B}} + \frac{\rho_{\mathrm{c}}^{n}\theta_{\mathrm{c}}\Omega}{\Delta t}\phi_{\mathrm{P}}^{n} + Q_{\phi}^{\mathrm{H}}. \end{aligned} \tag{38}$$

The algebraic equations are solved by the Alternating Direction Implicit method with Tridiagonal Matrix Algorithm or Bi-Conjugate Gradients Stablized Method [74] in this study.

3.6. Pressure-velocity coupling

In the incompressible Navier–Stokes equations, pressure and velocity are decoupled as the pressure term does not appear in the continuity equation. For some numerical discretisations this may cause convergence problems. However, when a staggered mesh is used, as in this work, coupling occurs as a result of the discretisation, as velocity updates on cell faces contain pressure terms. In this study, the SIMPLE algorithm [43] is employed for the pressure-velocity coupling, and more details can be found in [75]. SIMPLE algorithm is used to calculate the corrected pressure and after solving the pressure correction equation, the updated pressure and velocity are added by the pressure and velocity correction terms, respectively.

3.7. Volume of Fluid scheme for interface capturing

A key requirement for modelling two-phase flow is a method of calculating the shape of the interface. Numerous methods have been proposed and used for the simulation of interfacial flows. However, the VOF method for tracking the interface is one of the most popular approaches because of its advantages: mass conservation, computational efficiency and easy implementation. From a general point of view, there are two classes of algorithms to solve the F transport Equation (9): algebraic and geometric computation [76]. Excellent reviews on the VOF methods can be found in [22, 76].

Considering the advantages of the VOF method and efficiency in algebraic computation, the high resolution VOF scheme Compressive Interface Capturing Scheme for Arbitrary Meshes (CICSAM) is employed in this study to capture the air-water interface for breaking waves. CICSAM is a high resolution scheme based on the normalised variable diagram used by Leonard [77]. It contains two

DOI: 10.1002/fld

high resolution schemes, and the weighting factor is based on the angle between the interface and the direction of motion. An outline of CICSAM is given below. Refer to [44] for the details.

The normalised variable $\tilde{F}$ is defined as

$$\tilde{F} = \frac{F - F_{\mathrm{U}}}{F_{\mathrm{A}} - F_{\mathrm{U}}}, \tag{39}$$

where the subscript A indicates the acceptor and U the upwind cell. The Hyper-C scheme [77], which follows the upper bound of the convection boundedness criteria (CBC) is used as it is highly compressive and can convert a smooth gradient into a sharp step.

$$\tilde{F}_{\mathrm{f_{CBC}}} = \begin{cases} \min\left\{1, \dfrac{\tilde{F}_{\mathrm{D}}}{c_{\mathrm{D}}}\right\}, & \text{when } 0 \leqslant \tilde{F}_{\mathrm{D}} \leqslant 1 \\ \tilde{F}_{\mathrm{D}}, & \text{when } \tilde{F}_{\mathrm{D}} < 0, \tilde{F}_{\mathrm{D}} > 1 \end{cases} \tag{40}$$

where subscript D indicates donor cell, $c_{\mathrm{D}} = \sum_{\mathrm{f}} \max\left\{\frac{-V_{\mathrm{f}}\Delta t}{\Omega_{\mathrm{D}}}, 0\right\}$ is the Courant number of the donor cell and V_{f} is the volumetric flux. However, the Hyper-C scheme is inadequate to preserve the shape of an interface that lies tangentially to the flow direction. Thus CICSAM switches to the ULTIMATE-QUICKEST (UQ) scheme [77]

$$\tilde{F}_{\mathrm{f_{UQ}}} = \begin{cases} \min\left\{\dfrac{8c_{\mathrm{D}}\tilde{F}_{\mathrm{D}} + (1 - c_{\mathrm{D}})(6\tilde{F}_{\mathrm{D}} + 3)}{8}, \tilde{F}_{\mathrm{f_{CBC}}}\right\}, & \text{when } 0 \leqslant \tilde{F}_{\mathrm{D}} \leqslant 1 \\ \tilde{F}_{\mathrm{D}}, & \text{when } \tilde{F}_{\mathrm{D}} < 0, \tilde{F}_{\mathrm{D}} > 1 \end{cases} \tag{41}$$

in this case.

Thus, depending on the angle between the interface and the flow, CICSAM combines these two schemes, then

$$\tilde{F}_{\mathrm{f}} = \gamma_{\mathrm{f}}\tilde{F}_{\mathrm{f_{CBC}}} + (1 - \gamma_{\mathrm{f}})\tilde{F}_{\mathrm{f_{UQ}}}, \tag{42}$$

in which the weighting factor is given as

$$\gamma_{\mathrm{f}} = \min\left\{k_{\gamma}\frac{\cos(2\alpha_{\gamma}) + 1}{2}, 1\right\}, \tag{43}$$

where k_{γ} is a constant introduced to control the dominance of the different schemes and the recommended value is $k_{\gamma} = 1$, α_{γ} is the angle between the vector normal to the interface and the vector that convects the centres of donor and acceptor cells.

The final expression for the face value of F is

$$F_{\mathrm{f}} = (1 - \beta_{\mathrm{f}})F_{\mathrm{D}} + \beta_{\mathrm{f}}F_{\mathrm{A}}, \tag{44}$$

where the weight factor β_{f} is obtained by

$$\beta_{\mathrm{f}} = \frac{\tilde{F}_{\mathrm{f}} - \tilde{F}_{\mathrm{D}}}{1 - \tilde{F}_{\mathrm{D}}}. \tag{45}$$

It is noted that the normalised variable in Equation (39) will be divided by zero if the volume fraction F has the same value in the acceptor and upwind cell. In the numerical implementation, the numerator and denominator of the weighting factor in Equation (45) are multiplied by $(F_{\mathrm{A}} - F_{\mathrm{U}})$, resulting a modified expression of the normalised variable on the face (not shown here), to avoid the singularity in the computation.

DOI: 10.1002/fld

4. RESULTS AND DISCUSSION

4.1. Breaking waves on a sloping beach

In this section, we simulate a two-dimensional overturning solitary wave and compare both quantitatively and qualitatively with the experiment [78] for a breaking solitary wave splash-up on a 1:15 sloping beach. A number of different numerical methods have been developed to study this problem, such as the boundary element method (BEM) [20], coupling of BEM and VOF methods [79, 80], Corrected Incompressible Smoothed Particle Hydrodynamics method [41] and MLPG_R method [42].

In the simulation, the computational setup is the same as the laboratory setup except that we use the analytical solution to generate the solitary wave at the inlet. The schematic of the run-up of a breaking solitary wave is shown in Figure 5, where the origin of the coordinate system is on the still water level above the toe of the beach, x and z are the horizontal and vertical coordinates, respectively, D is the still water depth, H is the solitary wave height. The slope of the beach $\tan(\beta) = 1:15$, the still water depth is $D = 0.3048$ m, and we calculate the case for the incident solitary wave with the ratio of wave height to still water depth, $H/D = 0.45$. The computational domain starts from the toe of the beach and extends to the location beyond the maximum run-up point $18.75D$. The height of the computational domain is $1.75D$, and it is discretised by a 1800×140 nonuniform grid with minimum meshes $\Delta x/D = 0.005$ and $\Delta z/D = 0.005$ in the breaking region. At the inlet, the solitary wave is generated by giving the water surface profile and the water particle velocities based on the analytical solution [81] as

$$
\begin{aligned}
\eta(x,t) &= H\,\mathrm{sech}^2\left[\sqrt{\frac{3H}{4D^3}}X\right],\\
X &= x - Ct - x_L,\\
u(x,z,t) &= C\left\{\left[\frac{H}{D}+3\left(\frac{H}{D}\right)^2\left(\frac{1}{6}-\frac{1}{2}\left(\frac{z+D}{D}\right)^2\right)\right]\frac{\eta}{H}-\left(\frac{H}{D}\right)^2\left(\frac{7}{4}-\frac{9}{4}\left(\frac{z+D}{D}\right)^2\right)\left(\frac{\eta}{H}\right)^2\right\},\\
w(x,z,t) &= C\sqrt{\frac{3H}{D}}\frac{z+D}{D}\frac{\eta}{D}\tanh\left(\sqrt{\frac{3H}{4D^3}}X\right)\left\{1+\frac{H}{2D}\left[1-7\frac{\eta}{H}-\left(\frac{z+D}{D}\right)^2\left(1-\frac{3\eta}{H}\right)\right]\right\}.
\end{aligned}
\tag{46}
$$

The no-slip wall boundary condition is applied at the sloping beach and zero-gradient boundary conditions are applied at the top and outlet of the computational domain.

In Figure 6, the profiles of the overturning wave are quantitatively compared with the experimental data [78] at $t\sqrt{g/D} = 9.29, 9.87, 10.35, 10.73$ along with the recently published results of [42] using the MLPG_R method. At $t\sqrt{g/D} = 9.29$ before wave breaking, it can be seen that the wave crest becomes steep because of the shoaling effect. At $t\sqrt{g/D} = 9.87$ during wave breaking, the wave has passed the breaking point, which is defined as when the front of the wave becomes vertical and starts to overturn. At $t\sqrt{g/D} = 10.35$ during wave overturning, a plunging jet is formed in front of the wave. At $t\sqrt{g/D} = 10.73$ during wave curling down, the plunging jet will impinge the water surface ahead and generate the splash-up. It can be seen from Figure 6 that the computational

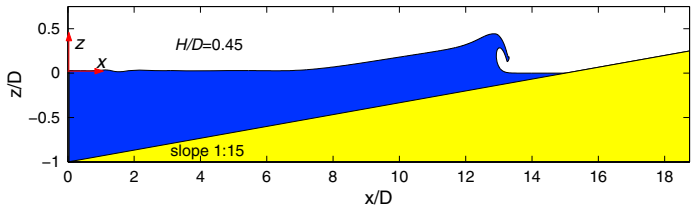

Figure 5. Schematic of an incident $H/D = 0.45$ solitary wave breaking on a 1:15 sloping beach (not scaled).

DOI: 10.1002/fld

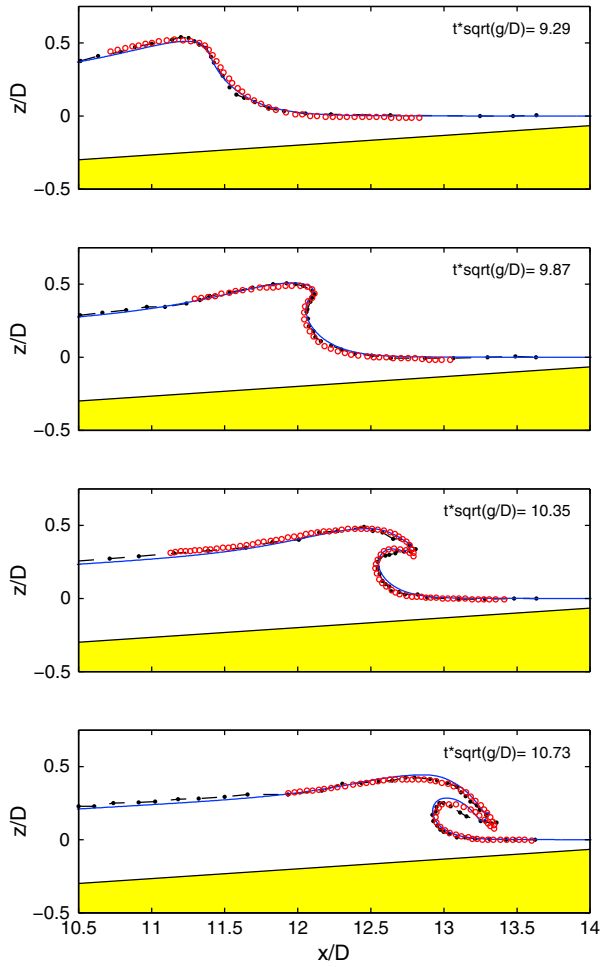

Figure 6. Quantitative comparison of wave surface profiles during wave overturning on a sloping beach for $H/D = 0.45$. Blue solid line, present results; red circles, experimental data [78]; black dashed line, results obtained by the MLPG_R method [42].

results agree well with experimental measurements and MLPG_R results in terms of the wave shape and location before wave curling down, and there is only a slight difference in the size of the cavity enclosed by the plunging jet. The slight discrepancy may be caused by the solitary wave at the inlet generated from the analytical solution differing slightly from the experiment [82].

A detailed comparison of the plunging jet, at the time of jet impingement, with the experimental and the BEM results are shown in Figure 7. Both numerical results (VOF and BEM) agree reasonably with experimental data. The slight difference is that the jet obtained from the VOF model has a similar size to that obtained from the BEM model and both are thicker than their experimental counterpart as discussed in [83]. Nevertheless, because the numerical model cannot get the exact initial condition used in the experiment, any small difference will lead to the change of the plunging jet, thus we do not expect to match everything between the experiment and computation. In an overall sense, the present code well predicts the overturning wave and a good agreement with experimental data is obtained.

The overturning jet of breaking waves has been investigated mathematically in [84–86]. New [85] has found that a certain section of the wave profile beneath overturning waves, in both deep and shallow water, can be closely approximated by a $\sqrt{3}$ aspect-ratio ellipse. The best fitted $\sqrt{3}$ aspect-ratio ellipse for the curve beneath the plunging jet obtained from the present model is also shown in Figure 7 with $-30°$ orientation relative to the x direction. It can be seen that the plunging

DOI: 10.1002/fld

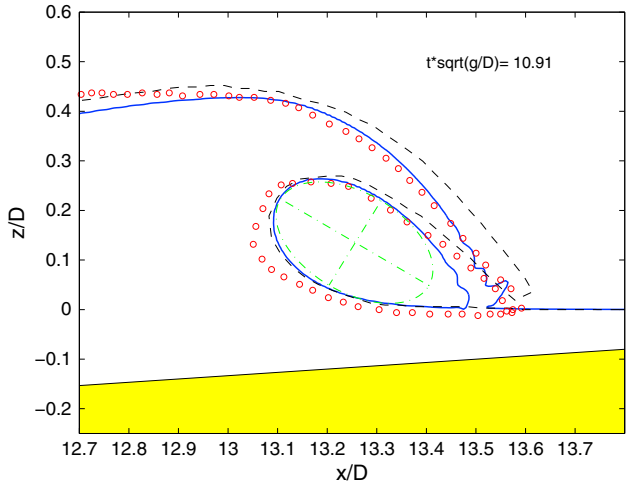

Figure 7. Detailed comparison of the plunging jet. Blue solid line, present results; red circles, experimental data [78]; black dashed line, profile at $t\sqrt{g/D} = 10.73$ obtained by the Boundary Element Method [20]; green dash-dotted line is a $\sqrt{3}$ aspect-ratio ellipse.

jet follows New's theory, and similar results have also been observed for deep-water breaking waves in the numerical simulations in [26, 27].

To investigate the convergence of the method, another two sets of mesh, a coarse mesh (900×90) with minimum meshes $\Delta x/D = 0.01$ and $\Delta z/D = 0.01$ and a fine mesh (2600×240) with minimum meshes $\Delta x/D = 0.0025$ and $\Delta z/D = 0.0025$, are used to simulate the overturning wave. The comparison of the profiles of the overturning wave is shown in Figure 8. It is found that the results are convergent, and grid-independent results are obtained for the medium and fine meshes. The finer mesh produces sharper plunging jet during wave overturning, but it requires more computational effort.

Figure 9 shows the velocity fields for both air and water during wave overturning. At $t\sqrt{g/D} = 9.29$ before wave breaking, the wave becomes steep, and the velocity in the water increases from the bottom to the water surface. The velocity and the water surface profile all suggest the wave is in the pre-breaking region, which is classified as $u < C$ before wave breaking. At $t\sqrt{g/D} = 9.87$

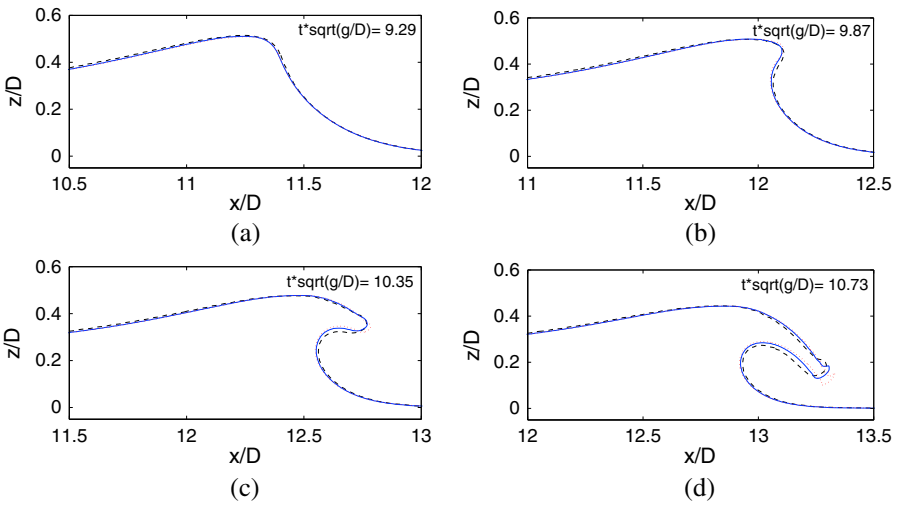

Figure 8. Comparison of the profiles of the overturning wave obtained by different meshes. Coarse mesh (900×90), black dashed line; medium mesh (1800×140), blue solid line; fine mesh (2600×240), red dotted line.

DOI: 10.1002/fld

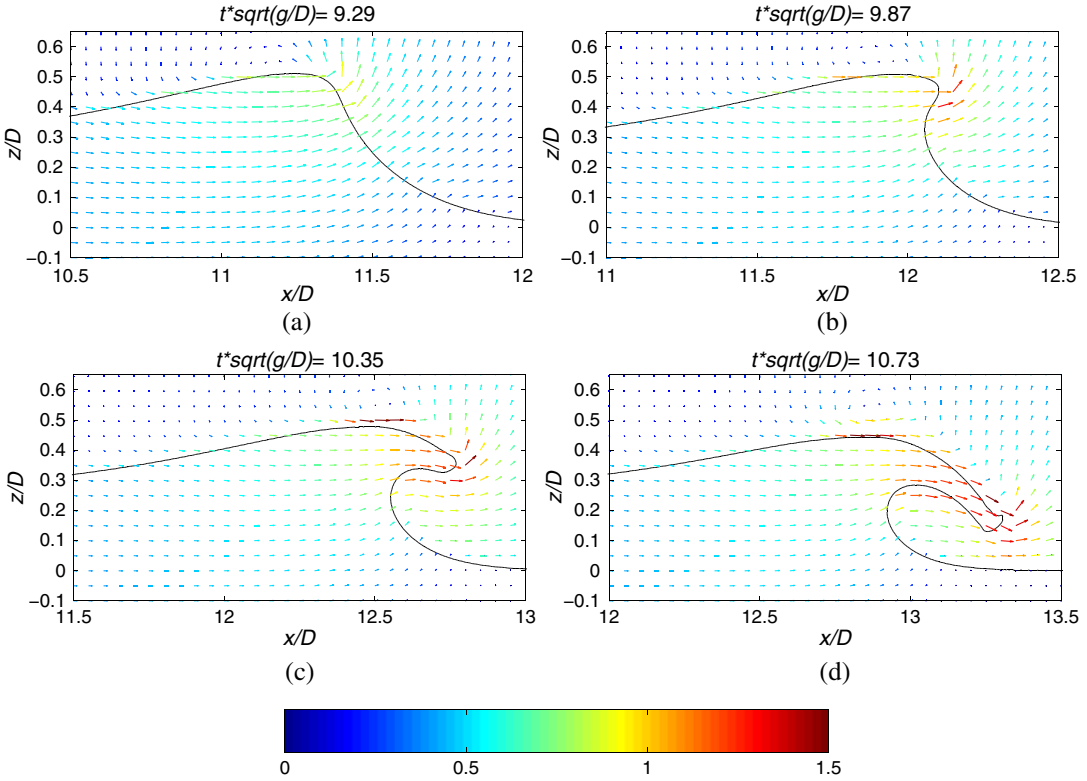

Figure 9. Velocity fields during wave overturning on a sloping beach. Velocities are normalised by the wave phase speed C, and the colour bar represents the magnitude of the velocity.

during wave breaking, the maximum velocity in the water is greater than the phase speed C, is nearly horizontal and is located at the front face of the wave. Large velocity vectors are produced in the air ahead of the front face of the wave because of the pushing of the wave. At $t\sqrt{g/D} = 9.87$ during wave overturning, the velocity in the plunging jet increases. At $t\sqrt{g/D} = 10.73$ during wave curling down, the maximum velocity in the water is located at the tip of the plunging jet and large velocities beneath the plunging jet are observed as the entrapped air tries to escape from the enclosed cavity. It is worth noting that the air above the crest of the wave tries to follow the water surface and the recirculation of air can be clearly observed above the wave crest during wave breaking. These results are more detailed than the experimental measurements [78] which cannot give velocities there. They are physically realistic so support the model to simulate breaking waves.

It is noted that numerical results are only presented up to the breaking process in Figure 6 because the measured water surface profiles are not available after the wave touches down for the case ($H/D = 0.45$). In order to show the capability of the present model in simulating wave post-breaking and subsequent splash-up processes, the case for the breaking solitary wave with $H/D = 0.4$ is computed with the same above mentioned computational setup, and quantitatively compared with the laboratory photographs [78, 87] in Figure 10. It can be seen that the development of plunging jet, jet impingement and generation of splash-up are reproduced in the simulation, which reasonably agree with the experimental measurements. However, there is a discrepancy between the simulation and experiment for the enclosed cavity and the secondary jet generated during the splash-up process. This is attributed to the strong two-phase flow mixing and the generation of small bubbles during the splash-up process, which is difficult to be simulated in the present model.

4.2. Breaking waves over a reef

It is worth pointing out that several researchers in [88] have used the overturning of a solitary wave over a reef [89] to validate their models, in which only the time series of water surface profiles at

DOI: 10.1002/fld

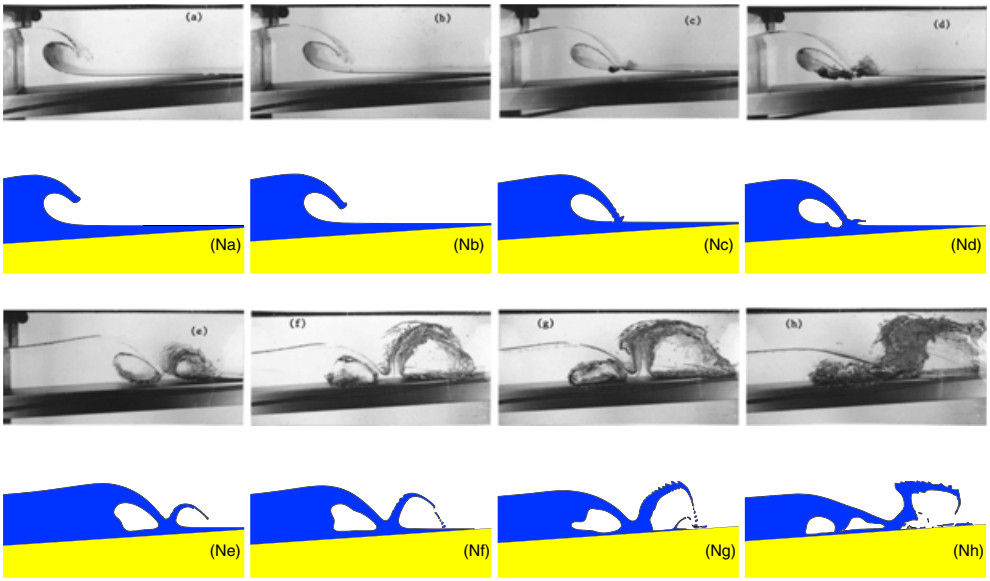

Figure 10. Qualitative comparison of numerical snapshots (Na-Nh) with laboratory photographs (a-h) [78, 87] (With permission from ASCE) for $H/D = 0.4$.

fixed gauges are compared against experimental data. In order to compare the model with others, we present our numerical results here for completeness.

We use a similar computational setup to [88]. The detail of the experimental setup can be found in [89]. The schematic of the overturning of a solitary wave over a reef is shown in Figure 11, where the origin of the coordinate system is on the still water level above the toe of the reef, x and z are the horizontal and vertical coordinates, respectively. $D = 0.31$ m is the still water depth, $H = 0.1314$ m is the solitary wave height, $R = 0.263$ m is the height of the reef. The computational domain is 6 m long and 0.8 m high, and it is discretised by a 1500×200 uniform grid. The no-slip boundary conditions are used for all boundaries, and the solitary wave is initialised similar to that in the previous section, but the centre is located at $x = -2$ m.

Figure 12 shows the comparison of wave elevations between numerical results and experimental data for the wave gauges P2-P4. At gauge P2 ($x = 0$ m), the wave profile is similar to the initial solitary wave, but the wave steepness is higher than that for the initial wave ($H/D = 0.424$). When the wave propagates on the reef, the wave profile becomes asymmetrical (see from P3 and P4) and the front of the wave becomes steeper during wave breaking. It is shown that the computed water surface profiles agree well with the experimental measurements [89], and similar to the results obtained in previous numerical studies [42, 88].

At the beginning of the solitary wave propagating towards the reef, there is little change in the wave shape. As the solitary wave approaches the toe of the reef, a small part of the wave is reflected

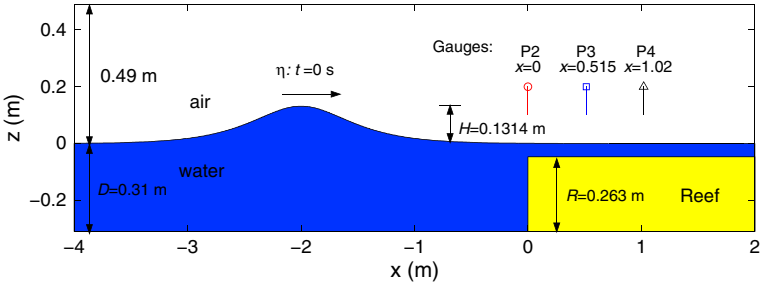

Figure 11. Schematic of the overturning of a solitary wave over a reef.

DOI: 10.1002/fld

back, whereas the main part of the wave propagates on the reef. Because the top of the wave moves faster than the bottom of the wave, the front of the wave is steepened, and the wave starts to overturn. Figure 13 shows the evolution of water surface profiles during wave overturning. At the onset of wave breaking ($t = 1.2$ s), the wave front becomes near vertical. The plunging jet is observed during wave overturning ($t = 1.3$ s and $t = 1.4$ s). The plunging jet impinges the water surface ahead to generate the secondary jet ($t = 1.6$ s) and the jet-splash cycles are developed afterwards ($t = 1.8$ s). The wave profiles at the breaking point and the jet-fall initiation, measured with a high-speed video

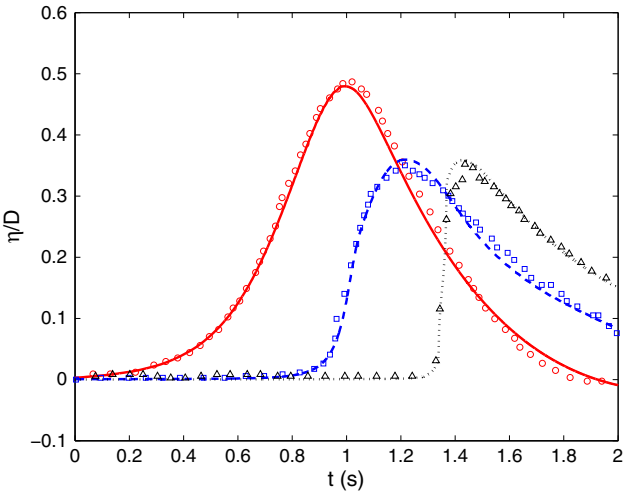

Figure 12. Comparison of wave elevations between numerical results (lines) and experimental data (marks). Wave gauges P2 (red), P3 (blue) and P4 (black). As the wave starts at a different location between the experiment and calculation, all experimental data are shifted with a same period of time to match the wave elevation in the first gauge P2.

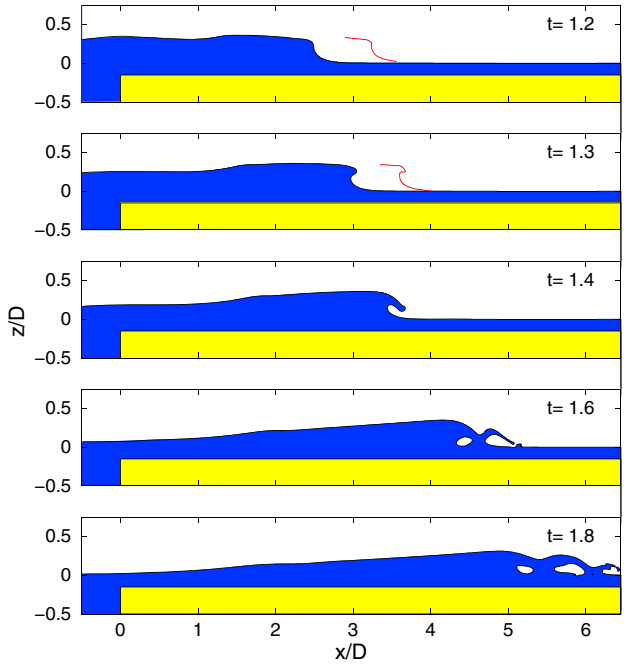

Figure 13. The evolution of water surface profiles during wave overturning over a reef. The experimental water surface profiles measured with the high-speed video camera during the overturning process are plotted in red lines (only two profiles at the breaking point and jet fall initiation are available in the experiment [89]).

DOI: 10.1002/fld

camera in [89], are plotted in Figure 13 as well for comparison. It is noted that the shape of the computed wave profiles reasonably agree with the experimental measurements, however, there is a phase shift between the numerical results and experimental data, which has also been observed in [90]. This might be attributed to the small domain used in the simulation, whereas a much longer domain was used in the experiment. Overall, the present model is capable of simulating the wave overturning, air entrainment and splash-up processes.

4.3. Breaking waves in deep water

Several numerical studies of deep-water breaking waves have been done in the past [26, 27, 29, 90, 91]. In these studies, a steep Stokes wave, which leads to a plunging breaker, was simulated in a periodic space domain. The same computational setup in [26, 29] is used here and the schematic of deep-water breaking waves is shown in Figure 14, where the wavelength (L) is taken as a reference length and $D/L = 0.5$. The computational domain is one wavelength wide and one wavelength high, that is $x/L, z/L \in [-0.5, 0.5]$, and is discretised by a 256×256 uniform grid. Periodic boundary conditions are imposed at the inlet and outlet of the computational domain, where the wave moves out of the right of the domain and will reenter from the left. No-slip boundary conditions are applied at the bottom and top of the domain. At $t = 0$, the water surface profile and water particle velocities for the Stokes wave are initialised as

$$\begin{aligned} \eta(x,0) &= \frac{a}{L}\left(\cos(k^{\mathrm{w}}x) + \frac{1}{2}\xi\cos(2k^{\mathrm{w}}x) + \frac{3}{8}\xi^2\cos(3k^{\mathrm{w}}x)\right), \\ u(x,z,0) &= a\sqrt{gk^{\mathrm{w}}(1+\xi^2)}\exp(k^{\mathrm{w}}y)\cos(k^{\mathrm{w}}x), \\ w(x,z,0) &= a\sqrt{gk^{\mathrm{w}}(1+\xi^2)}\exp(k^{\mathrm{w}}y)\sin(k^{\mathrm{w}}x), \end{aligned} \tag{47}$$

in which a is the wave amplitude, $k^{\mathrm{w}} = 2\pi/L$ is the wavenumber, $\xi = ak^{\mathrm{w}}$ is the wave steepness and $\xi = 0.55$ is considered here.

Figure 15 shows the space-time evolution of water surface profiles during wave breaking. It can be seen that the front of the wave is steepened during wave propagation, a plunging breaker is developed when the wave reenters the domain from the left ($x/L = -0.5$). The plunging jet impinges the water surface ahead, and jet-splash cycles are observed afterwards, similar to overturning waves in shallow water (see Figure 10 and Figure 13). It is shown that the deep-water breaking waves are captured by the present model and similar to previous published results.

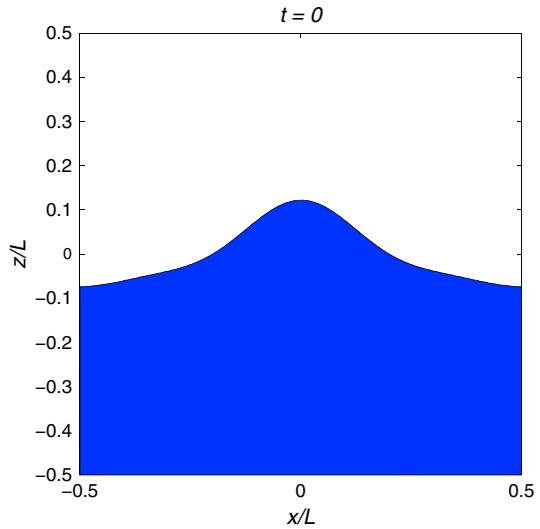

Figure 14. Schematic of breaking waves in deep water.

DOI: 10.1002/fld

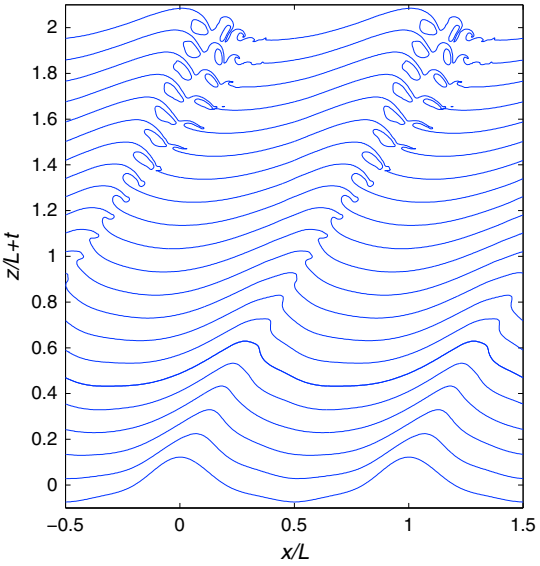

Figure 15. The space-time evolution of water surface profiles during wave breaking in deep water. For the sake of clarity, the numerical results are also mapped into the interval $x \in [0.5, 1.5]$.

5. CONCLUSIONS

In this study, a two-phase flow model has been developed for investigating breaking waves in both deep and shallow water, focusing on the wave overturning and post-breaking processes. The model is based on the RANS equations with the $k-\epsilon$ turbulence model. The finite volume method is utilised to discretise spatial derivatives and a backward finite difference discretisation was used for the time derivative, which lead to an implicit scheme for the governing equations. The SIMPLE algorithm is employed for the pressure-velocity coupling, the Cartesian cut-cell method is implemented to deal with complex geometries, and the air-water interface was captured by the high resolution VOF scheme CICSAM.

In order to validate the model, overturning waves on a sloping beach and over a reef were computed and compared with available experimental data. It is shown that good agreement between numerical simulations and experimental measurements for the water surface profiles was obtained using the two-phase flow model presented here. Furthermore, deep-water breaking waves in a periodic domain was simulated and similar results were obtained with previous studies. The overturning jet, air entrainment and splash-up during wave breaking have been captured by the two-phase flow model, which demonstrates the capability of the model to simulate free surface flow and wave breaking problems.

Although only two-dimensional (2D) wave breaking over simple geometries (sloping beach and reef) is considered here, this study should be regarded as a first step towards better understanding of the kinematics and dynamics of breaking waves. Because of complex processes during wave breaking, much future effort should be devoted to further this study. One aspect is to extend this model for more realistic three-dimensional (3D) breaking waves, in which the generation of turbulence and vortex structures are different from that in 2D breaking waves. Compared with the 2D case, the spanwise variation of the wave during propagation can be taken into account in the 3D simulation, which would better represent the actual wave breaking process seen in nature. The 3D wave profile could be observed during the wave breaking process, in which the wave can break first at some points and continue with spreading laterally. The flow field may become more obviously three-dimensional especially during air entrainment and jet-splash cycles after wave breaking. Furthermore, the generation of obliquely descending eddies could be observed in the 3D simulation. Another aspect is to investigate breaking waves over more complex topography, such as convex and concave coastlines. Water waves change their direction during wave propagation because of wave

DOI: 10.1002/fld

refraction and diffraction over a varying bathymetry. As the waves shoal in shallow water, fully 3D breaking waves develop and earlier or later wave breaking will be observed at different lateral locations depending on the local wave steepness. Studies on these two aspects, which will improve our understanding of the characteristics of 3D breaking waves, are currently underway and will be reported in the near future.

ACKNOWLEDGEMENTS

The author would like to acknowledge the financial support by the Marie Curie EST fellowship for his PhD study at the University of Leeds. Drs Xianyun Wen and Andrew N. Ross are greatly appreciated for their guidance and advice. Special thanks are due to Dr Matthew Hubbard and Prof. Peter Jimack for providing useful comments and suggestions. Invaluable comments from anonymous reviewers for the improvement of the manuscript are also gratefully acknowledged.

REFERENCES

1. Peregrine DH. Breaking waves on beaches. *Annual Review of Fluid Mechanics* 1983; **15**:149–178.
2. Banner ML, Peregrine DH. Wave breaking in deep-water. *Annual Review of Fluid Mechanics* 1993; **25**:373–397.
3. Battjes JA. Surf-zone dynamics. *Annual Review of Fluid Mechanics* 1988; **20**:257–293.
4. Mei CC, Liu PLF. Surface-waves and coastal dynamics. *Annual Review of Fluid Mechanics* 1993; **25**:215–240.
5. Duncan JH. The breaking and non-breaking wave resistance of a two-dimensional hydrofoil. *Journal of Fluid Mechanics* 1983; **126**:507–520.
6. Lin JC, Rockwell D. Evolution of a quasi-steady breaking wave. *Journal of Fluid Mechanics* 1995; **302**:29–44.
7. Bonmarin P. Geometric-properties of deep-water breaking waves. *Journal of Fluid Mechanics* 1989; **209**:405–433.
8. Rapp RJ, Melville WK. Laboratory measurements of deep-water breaking waves. *Philosophical Transactions of the Royal Society of London Series A-Mathematical Physical and Engineering Sciences* 1990; **331**(1622):735–800.
9. Perlin M, He JH, Bernal LP. An experimental study of deep water plunging breakers. *Physics of Fluids* 1996; **8**(9):2365–2374.
10. Tulin MP, Waseda T. Laboratory observations of wave group evolution, including breaking effects. *Journal of Fluid Mechanics* 1999; **378**:197–232.
11. Melville WK, Veron F, White CJ. The velocity field under breaking waves: coherent structures and turbulence. *Journal of Fluid Mechanics* 2002; **454**:203–233.
12. Nadaoka K, Hino M, Koyano Y. Structure of the turbulent-flow field under breaking waves in the surf zone. *Journal of Fluid Mechanics* 1989; **204**:359–387.
13. Ting FCK, Kirby JT. Observation of undertow and turbulence in a laboratory surf zone. *Coastal Engineering* 1994; **24**(1-2):51–80.
14. Kimmoun O, Branger H. A particle image velocimetry investigation on laboratory surf-zone breaking waves over a sloping beach. *Journal of Fluid Mechanics* 2007; **588**:353–397.
15. Titov VV, Synolakis CE. Modeling of breaking and nonbreaking long-wave evolution and runup using VTCS-2. *Journal of Waterway, Port, Coastal, and Ocean Engineering-ASCE* 1995; **121**(6):308–316.
16. Li Y, Raichlen F. Non-breaking and breaking solitary wave run-up. *Journal of Fluid Mechanics* 2002; **456**:295–318.
17. Zelt JA. The run-up of nonbreaking and breaking solitary waves. *Coastal Engineering* 1991; **15**(3):205–246.
18. Longuet-Higgins MS, Cokelet ED. The deformation of steep surface-waves on water. Part 1. Numerical method of computation. *Proceedings of the Royal Society of London Series A-Mathematical Physical and Engineering Sciences* 1976; **350**(1660):1–26.
19. Dommermuth DG, Yue DKP, Lin WM, Rapp RJ, Chan ES, Melville WK. Deep-water plunging breakers - a comparison between potential-theory and experiments. *Journal of Fluid Mechanics* 1988; **189**:423–442.
20. Grilli ST, Svendsen IA, Subramanya R. Breaking criterion and characteristics for solitary waves on slopes. *Journal of Waterway, Port, Coastal, and Ocean Engineering-ASCE* 1997; **123**(3):102–112.
21. Yan S, Ma QW. QALE-FEM for modelling 3D overturning waves. *International Journal for Numerical Methods in Fluids* 2010; **63**(6):743–768.
22. Scardovelli R, Zaleski S. Direct numerical simulation of free-surface and interfacial flow. *Annual Review of Fluid Mechanics* 1999; **31**:567–603.
23. Miyata H. Finite-difference simulation of breaking waves. *Journal of Computational Physics* 1986; **65**(1):179–214.
24. Rhee SH, Stern F. RANS model for spilling breaking waves. *Journal of Fluids Engineering-Transactions of the ASME* 2002; **124**(2):424–432.
25. Iafrati A, Campana EF. Free-surface fluctuations behind microbreakers: space-time behaviour and subsurface flow field. *Journal of Fluid Mechanics* 2005; **529**:311–347.
26. Chen G, Kharif C, Zaleski S, Li J. Two-dimensional Navier-Stokes simulation of breaking waves. *Physics of Fluids* 1999; **11**(1):121–133.
27. Hendrickson KL. Navier-Stokes simulation of steep breaking water waves with a coupled air-water interface. *Ph.D. Thesis*, Massachusetts Institute of Technology, 2005.

DOI: 10.1002/fld

28. Lubin P, Vincent S, Abadie S, Caltagirone JP. Three-dimensional large eddy simulation of air entrainment under plunging breaking waves. *Coastal Engineering* 2006; **53**(8):631–655.
29. Iafrati A. Numerical study of the effects of the breaking intensity on wave breaking flows. *Journal of Fluid Mechanics* 2009; **622**:371–411.
30. Lin P, Liu PLF. A numerical study of breaking waves in the surf zone. *Journal of Fluid Mechanics* 1998; **359**:239–264.
31. Bradford SF. Numerical simulation of surf zone dynamics. *Journal of Waterway, Port, Coastal, and Ocean Engineering-ASCE* 2000; **126**(1):1–13.
32. Zhao Q, Armfield S, Tanimoto K. Numerical simulation of breaking waves by a multi-scale turbulence model. *Coastal Engineering* 2004; **51**(1):53–80.
33. Christensen ED, Deigaard R. Large eddy simulation of breaking waves. *Coastal Engineering* 2001; **42**(1):53–86.
34. Watanabe Y, Saeki H, Hosking RJ. Three-dimensional vortex structures under breaking waves. *Journal of Fluid Mechanics* 2005; **545**:291–328.
35. Hieu PD, Katsutohi T, Ca VT. Numerical simulation of breaking waves using a two-phase flow model. *Applied Mathematical Modelling* 2004; **28**(11):983–1005.
36. Wang Z, Zou Q, Reeve DE. Simulation of spilling breaking waves using a two phase flow CFD model. *Computers & Fluids* 2009; **38**(10):1995–2005.
37. Guignard S, Marcer R, Rey V, Kharif C, Fraunie P. Solitary wave breaking on sloping beaches: 2-D two phase flow numerical simulation by SL-VOF method. *European Journal of Mechanics B-Fluids* 2001; **20**(1):57–74.
38. Koshizuka S, Nobe A, Oka Y. Numerical analysis of breaking waves using the moving particle semi-implicit method. *International Journal for Numerical Methods in Fluids* 1998; **26**(7):751–769.
39. Shao SD. Simulation of breaking wave by SPH method coupled with k-ϵ model. *Journal of Hydraulic Research* 2006; **44**(3):338–349.
40. Dalrymple RA, Rogers BD. Numerical modeling of water waves with the SPH method. *Coastal Engineering* 2006; **53**(2-3):141–147.
41. Khayyer A, Gotoh H, Shao SD. Corrected incompressible SPH method for accurate water-surface tracking in breaking waves. *Coastal Engineering* 2008; **55**(3):236–250.
42. Ma QW, Zhou JT. MLPG_R method for numerical simulation of 2D breaking waves. *CMES-Computer Modeling in Engineering and Sciences* 2009; **43**(3):277–303.
43. Patankar SV. *Numerical heat transfer and fluid flow*. Taylor & Francis,: London, 1980.
44. Ubbink O. Numerical prediction of two fluid systems with sharp interfaces. *Ph.D. Thesis*, Imperial College of Science, Technology and Medicine, 1997.
45. Launder BE, Spalding DB. The numerical computation of turbulent flows. *Computer Methods in Applied Mechanics and Engineering* 1974; **3**(2):269–289.
46. Lin P. Numerical modeling of breaking waves. *Ph.D. Thesis*, Cornell University, 1998.
47. Ferziger JH, Peric M. *Computational Methods for Fluid Dynamics* (3rd rev. edn). Springer: Berlin, 2002.
48. Hirsch C. *Numerical Computation of Internal and External Flows Introduction to the Fundamentals of CFD* (New edn.) Butterworth-Heinemann: Oxford, 2007.
49. Fadlun EA, Verzicco R, Orlandi P, Mohd-Yusof J. Combined immersed-boundary finite-difference methods for three-dimensional complex flow simulations. *Journal of Computational Physics* 2000; **161**(1):35–60.
50. Tseng YH, Ferziger JH. A ghost-cell immersed boundary method for flow in complex geometry. *Journal of Computational Physics* 2003; **192**(2):593–623.
51. Balaras E. Modeling complex boundaries using an external force field on fixed Cartesian grids in large-eddy simulations. *Computers & Fluids* 2004; **33**(3):375–404.
52. Mittal R, Iaccarino G. Immersed boundary methods. *Annual Review of Fluid Mechanics* 2005; **37**:239–261.
53. Udaykumar HS, Shyy W, Rao MM. ELAFINT: a mixed Eulerian-Lagrangian method for fluid flows with complex and moving boundaries. *International Journal for Numerical Methods in Fluids* 1996; **22**(8):691–712.
54. Ye T, Mittal R, Udaykumar HS, Shyy W. An accurate Cartesian grid method for viscous incompressible flows with complex immersed boundaries. *Journal of Computational Physics* 1999; **156**(2):209–240.
55. Tucker PG, Pan Z. A Cartesian cut cell method for incompressible viscous flow. *Applied Mathematical Modelling* 2000; **24**(8-9):591–606.
56. Ingram DM, Causon DM, Mingham CG. Developments in Cartesian cut cell methods. *Mathematics and Computers in Simulation* 2003; **61**(3-6):561–572.
57. Kirkpatrick MP, Armfield SW, Kent JH. A representation of curved boundaries for the solution of the Navier-Stokes equations on a staggered three-dimensional Cartesian grid. *Journal of Computational Physics* 2003; **184**(1):1–36.
58. Chung MH. Cartesian cut cell approach for simulating incompressible flows with rigid bodies of arbitrary shape. *Computers & Fluids* 2006; **35**(6):607–623.
59. Causon DM, Ingram DM, Mingham CG, Yang G, Pearson RV. Calculation of shallow water flows using a Cartesian cut cell approach. *Advances in Water Resources* 2000; **23**(5):545–562.
60. Kleefsman KMT, Fekken G, Veldman AEP, Iwanowski B, Buchner B. A Volume-of-Fluid based simulation method for wave impact problems. *Journal of Computational Physics* 2005; **206**(1):363–393.
61. Torrey MD, Cloutman LD, Mjolsness RC, Hirt CW. NASA-VOF2D: a computer program for incompressible flows with free surfaces. *Technical Report LA-10612-MS*, Los Alamos Scientific Laboratory, 1985.

DOI: 10.1002/fld

62. Lin P. A fixed-grid model for simulation of a moving body in free surface flows. *Computers & Fluids* 2007; **36**(3):549–561.
63. Roe PL. Characteristic-based schemes for the Euler equations. *Annual Review of Fluid Mechanics* 1986; **18**:337–365.
64. Waterson NP, Deconinck H. Design principles for bounded higher-order convection schemes - a unified approach. *Journal of Computational Physics* 2007; **224**(1):182–207.
65. Unverdi SO, Tryggvason G. A front-tracking method for viscous, incompressible, multi-fluid flows. *Journal of Computational Physics* 1992; **100**(1):25–37.
66. Udaykumar HS, Kan HC, Shyy W, TranSonTay R. Multiphase dynamics in arbitrary geometries on fixed Cartesian grids. *Journal of Computational Physics* 1997; **137**(2):366–405.
67. Rudman M. A volume-tracking method for incompressible multifluid flows with large density variations. *International Journal for Numerical Methods in Fluids* 1998; **28**(2):357–378.
68. Bussmann M, Kothe DB, Sicilian JM. Modeling high density ratio incompressible interfacial flows. In *ASME 2002 Joint U.S.-European Fluids Engineering Division Conference*. ASME: Montreal, Quebec, Canada, 2002; 707–713.
69. Prosperetti A, Tryggvason G. *Computational Methods for Multiphase Flow*. Cambridge University Press: Cambridge, 2007.
70. Esmaeeli A, Tryggvason G. A direct numerical simulation study of the buoyant rise of bubbles at O(100) Reynolds number. *Physics of Fluids* 2005; **17**(9):093303.
71. Mencinger J, Zun I. On the finite volume discretisation of discontinuous body force field on collocated grid: application to VOF method. *Journal of Computational Physics* 2007; **221**(2):524–538.
72. Wemmenhove R. Numerical simulation of two-phase flow in offshore environments. *Ph.D. Thesis*, University of Groningen, 2008.
73. Youngs DL. Time-dependent multi-material flow with large fluid distortion. In *Numerical Methods for Fluid Dynamics*, Morton KW, Baines MJ (eds). Academic: New York, 1982; 273–285.
74. van der Vorst HA. Bi-CGSTAB - a fast and smoothly converging variant of Bi-CG for the solution of nonsymmetric linear-systems. *SIAM Journal on Scientific and Statistical Computing* 1992; **13**(2):631–644.
75. Xie Z. Numerical modelling of breaking waves under the influence of wind. *Ph.D. Thesis*, University of Leeds, 2010.
76. Rider WJ, Kothe DB. Reconstructing volume tracking. *Journal of Computational Physics* 1998; **141**(2):112–152.
77. Leonard BP. The ultimate conservative difference scheme applied to unsteady one-dimensional advection. *Computer Methods in Applied Mechanics and Engineering* 1991; **88**(1):17–74.
78. Li Y. Tsunamis: Non-breaking and breaking solitary wave run-up. *Ph.D. Thesis*, California Institute of Technology, 2000.
79. Guignard S, Grilli ST, Marcer R, Rey V. Computation of shoaling and breaking waves in nearshore areas by the coupling of BEM and VOF methods. *Proceedings of the Ninth (1999) International Offshore and Polar Engineering Conference*, 1999; 304–309.
80. Lachaume C, Biausser B, Grilli ST, Fraunie P, Guignard SP. Modeling of breaking and post-breaking waves on slopes by coupling of BEM and VOF methods. *Proceedings of the Thirteenth (2003) International Offshore and Polar Engineering Conference,* vol. 3, 2003; 353–359.
81. Dean RG, Dalrymple RA. *Water wave mechanics for engineers and scientists*. Prentice-Hall: Englewood Cliffs, N. J., 1984.
82. Lee JJ, Skjelbreia JE, Raichlen F. Measurement of velocities in solitary waves. *Journal of Waterway, Port, Coastal, and Ocean Engineering-ASCE* 1982; **108**(2):200–218.
83. Li Y, Raichlen F. Discussion: breaking criterion and characteristics for solitary waves on slopes. *Journal of Waterway, Port, Coastal, and Ocean Engineering-ASCE* 1998; **124**(6):329–333.
84. Longuet-Higgins MS. Parametric solutions for breaking waves. *Journal of Fluid Mechanics* 1982; **121**:403–424.
85. New AL. A class of elliptical free-surface flows. *Journal of Fluid Mechanics* 1983; **130**:219–239.
86. Greenhow M. Free-surface flows related to breaking waves. *Journal of Fluid Mechanics* 1983; **134**:259–275.
87. Li Y, Raichlen F. Energy balance model for breaking solitary wave runup. *Journal of Waterway, Port, Coastal, and Ocean Engineering-ASCE* 2003; **129**(2):47–59.
88. Helluy P, Golay F, Caltagirone JP, Lubin P, Vincent S, Drevard D, Marcer R, Fraunie P, Seguin N, Grilli S *et al*. Numerical simulations of wave breaking. *ESAIM-Mathematical Modelling and Numerical Analysis-Modelisation Mathematique Et Analyse Numerique* 2005; **39**(3):591–607.
89. Yasuda T, Mutsuda H, Mizutani N. Kinematics of overturning solitary waves and their relations to breaker types. *Coastal Engineering* 1997; **29**(3-4):317–346.
90. Lubin P. Large eddy simulation of plunging breaking waves. *Ph.D. Thesis*, University of Bordeaux, 2004.
91. Song CY, Sirviente AI. A numerical study of breaking waves. *Physics of Fluids* 2004; **16**(7):2649–2667.

DOI: 10.1002/fld